Is a glacier gone when it looks gone? Subsurface characteristics of high-Arctic ice-cored slopes as evidence of the latest maximum glacier extent.

Éric Bernard *, Jean-Michel Friedt†, Alexander Prokop‡, Florian Tolle§, Madeleine Griselin ¶

March 22, 2024

1 Abstract

In the context of glacier retreat and increased precipitations, Arctic glacier basin slopes are subject to stress leading to visible transformations. In this work, sub-surface features of a small Arctic glacier basin slopes are mapped using Ground Penetrating RADAR. In combination with surface topography data, 8 transects were surveyed ranging from the areas furthest from the current glacier extent to the areas still in contact with the glacier. This allowed for a reconstitution of the successive stages ice-cored slopes go through when glaciers retreat. It appears that slopes evolve from thick debris-covered ice bodies connected with the glacier, to residual ice and ice/debris mixes covered in debris. At the same time, surface morphology of the slopes shifts from homogeneous ice-cored slope gradients to more complex talus-type slopes at the end of the process. The stages of these evolutions are in compliance with former glacier extents. The main driving factors of the slopes successive stages are the constant slope adjustments linked to debris movements, and the melting of ice cores. All these factors are exacerbated by the warmer and wetter conditions they are subject to.

Keywords: Slopes dynamics, Ground Penetrating Radar, Periglacial adjustment, Svalbard

*ThéMA, CNRS, France
†FEMTO-ST, Université de Franche-Comté, France
‡University of Vienna, Austria
§ThéMA, Univ. Franche Comté, France
¶ThéMA, CNRS, France

2 Introduction

Receding glacier dynamics left new spaces where processes typical of cold non-glacial environment are increasingly developing ([1, 2]). The glacier's ability to protect the underlying bedrock is weakening, resulting in the degradation of unconsolidated landforms (e.g. soil settlement, strong erosion and topographic reshaping) as highighted by [3, 4, 5]. Multiple studies [6, 7, 8] have shown that the periglacial processes resulting from climate change and glacial retreat have caused geomorphological changes in proglacial environments [9] and have particularly influenced slope adjustments [10, 11, 12].

Geomorphological changes are largely controlled by glacial retreat [13, 14, 15, 16, 17, 18, 6]. They are observed as slope geometry changes and the formation of fan-shaped landforms due to the abundance of easily mobilized materials [19, 20, 21, 22, 23]. Such landforms were identified during Autumn 2022 field trips. They are known to be associated with structures capable of preserving buried ice and are characterized by very steep fans formed by successive landslides [24, 25] and snow avalanches that have redeposited the debris torn from the slopes [26].

Previous observations have shown that, despite the visual appearance of being at the edge of the glacier, the ice extending from the glacier actually extends up the slopes surrounding the glacier basin [27]. However, the exact composition and structure of these proglacial slopes are not well understood. In this work, the maximum elevation of the buried ice is associated with past Holocene maximum thickness of the Auste Lovén (AL) glacier.

In this study, we are exploring how the slopes undergo changes both during and after the glacier retreat, as well as examining the glacial and periglacial heritage left behind from the Little Ice Age (LIA) maximum extent. Since the glacier continues to shrink, we observe a layer of debris formed by successive accumulations of rock falls. We thus examine the way in which ice (i.e., above the slopes and then covered with debris) evolves from the moment it is still part of the glacier to the stage where only buried ice bodies remain. Our focus is on areas ranging from the glacier front, to areas that have been disconnected from the glacier for at least a century since the end of the LIA. The goal of this study is to map sub-surface debris covered ice extent in the slopes and its connection with the main AL glacier body as it retreats.

This paper aims at i) highlighting the internal structure of slopes by considering the evolution of the buried ice bodies disconnected from the glacier, soon after the glacial retreat in order to ii) determine their potential transformation. This should allow to iii) assess past elevation of the glacier prior to the current melt. The study concludes that the thickest extent of the ice body can be recovered from the maps of buried ice in the slopes. Furthermore, we conclude that the main glacier body as delineated from aerial or satellite imagery extends deep into the slopes, holding a substantial amount of ice unaccounted for when measuring exposed areas only. While the oldest buried ice has become mixed with falling boulders, the most recently deglaciated areas exhibit a sharp interface of uniform ice covered with debris.

3 Geographical settings

This study focuses on a small Arctic glacial basin located on Brøgger peninsula in Svalbard, Norwegian high Arctic (Fig. 1 bottom-right), covering an area of 10.58 km^2. AL glacier is a land-terminating valley glacier with a mixed polythermal / cold nature. It has a maximum altitude of 550 m.a.s.l. in its highest accumulation cirque and covers an area of 4.5 km^2. Following a similar trend to other glaciers on the Brøgger peninsula, the mean ablation rate has increased over time. In the case of AL, the mean ablation rate has increased from 0.422 m.a^{-1} between 1962 and 1995 to 0.505 m.a^{-1} for the 1995—2013 period [28].

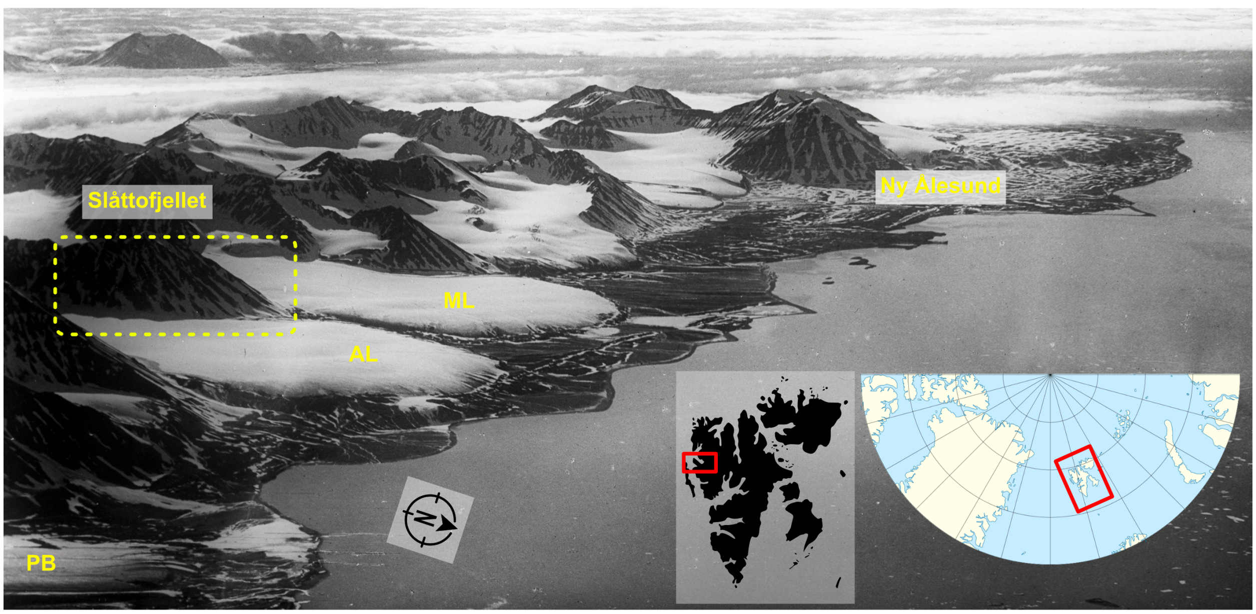

Figure 1: Historical aerial photography illustrating the maximum post-Little Ice Age extent of Brøggerhalvoya glaciers in 1923. Austre Lovénbreen (AL) is surrounded by Midtre Lovénbreen (ML, background) and Pedersenbreen (PB, foreground). The dashed square highlights the area of interest, in the slopes where AL and ML were once connected. Image in the public domain available from Wikimedia Commons.

AL is surrounded by Midtre Lovénbreen (ML) and Pedersenbreen (PB), but was only adjacent to ML once in the past as shown in Fig. 1 [29] and on historical maps [30]. The specific areas investigated in this paper are the slopes of the Slåttofjellet mountain between AL and ML. This area was selected following field observations where buried ice bodies have been first identified following landslides (S2).

4 Materials and methods

Based on the interpretation of aerial imagery from 1936, it has been deduced [31] that the AL glacier reached its Holocene maximum extent at the time this picture was shot (1936). The assumption leading to the conclusion that ice rose high in the slopes is supported by an oblique aerial photo (Fig. 2) showing the maximum ice extent and analyzed by various authors [32, 27, 33].

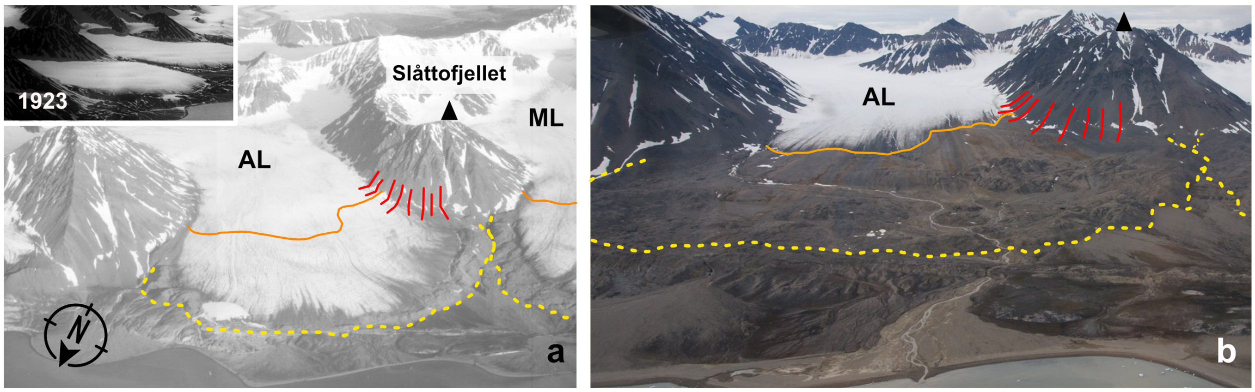

Figure 2: Comparison between 2 aerial pictures taken respectively in 1936 and in 2022. The solid lines expose the 2022 glacier limits. The dashed lines expose the maximum extent identified on the 1923 image for comparison in both contexts. Inset (a): excerpt of the 1923 picture focusing on AL at its maximum extent. The red lines show the Ground-Penetrating Radar transects carried out for this study. Left figure reference S36_1553 from Norsk Polar Institute reproduced with authorization.

Despite the different viewing angles, the images in Fig. 2 (right) clearly show the newly deglaciated areas, indicating that the slopes are now less influenced by glaciers. In Fig. 2 (left), the westernmost Ground Penetrating Radar (GPR) transect closest to ML reaches the historical limit of the maximum ice extent, which is now mostly deglaciated. This is more apparent in this picture compared to the 1923 image shown in Fig. 1.

For this study, inspired by aerial image analysis, we used LiDAR generated Digital Elevation Models (DEM) and analyzed the internal structure of the slopes through a detailed Ground-Penetrating Radar (GPR) survey of the mountainside.

A field measurement campaign was carried out in April 2023. Conducting the campaign when slopes are snow-covered was justified for safety reasons as the rocky slopes were otherwise unstable and unsafe. Moreover, it was easier to move the GPR antennas over the smooth, snow-covered slopes (Fig. 3) while the sledge to which antennas are fitted would be in close contact with the surface, allowing for the electromagnetic wave to efficiently couple with the ground.

The GPR data was collected using a Malå ProEx system fitted with shielded 500 MHz antennas. A custom

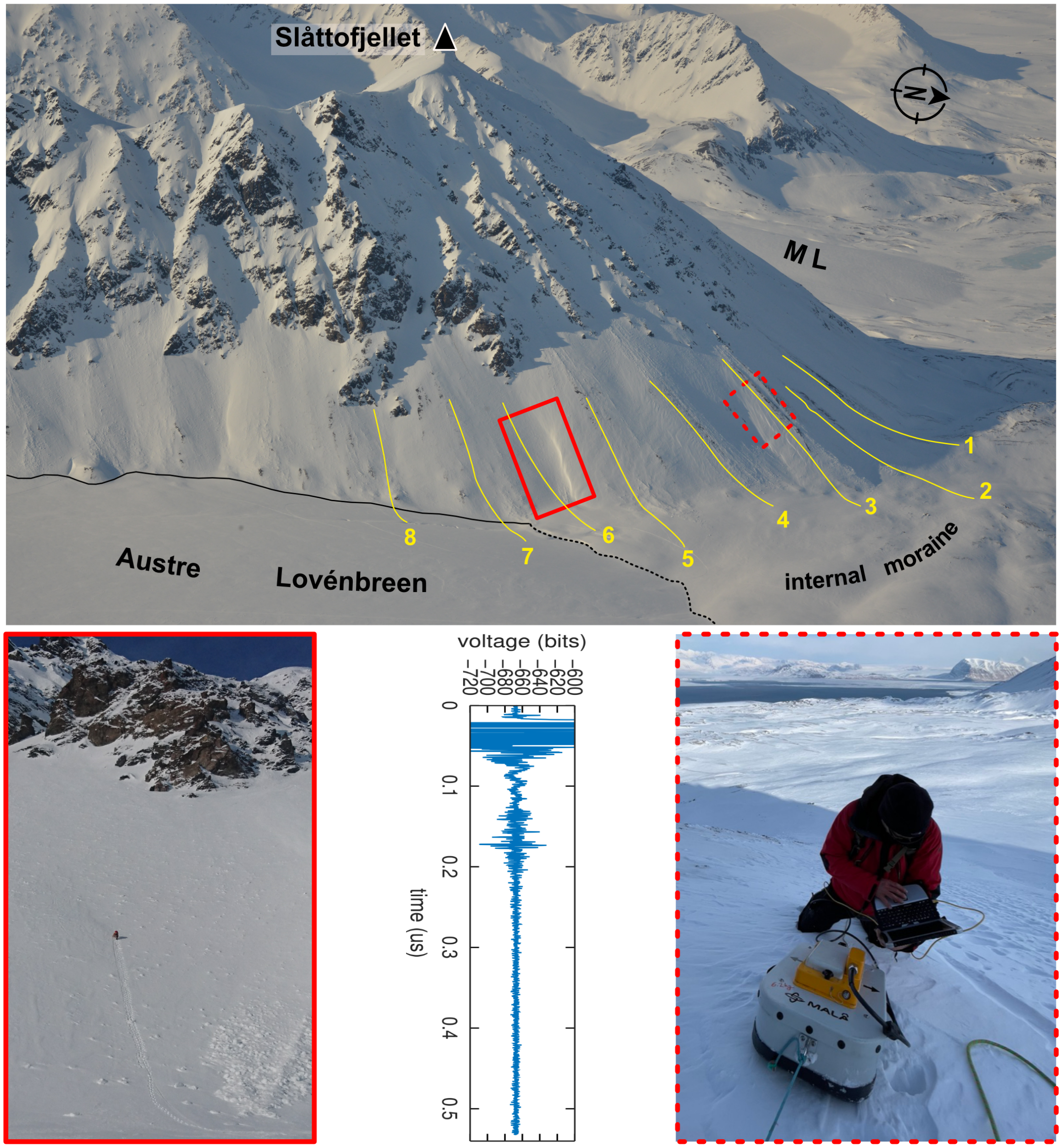

Figure 3: Top: picture taken from the Haavimbfjellet summit, opposite to Slåttofjellet from the right bank of AL highlighting the field of study field. The 8 transects (yellow lines) are located on the E-NE sides of the Slåttofjellet. The red solid square emphasizes on the bottom-left picture how the measurements were carried out using mountaineering techniques. The dashed square, focusing on the bottom-right picture highlights the whole setup with the operator on the slopes. Bottom-center: an example of raw GPR A-scan measurement collected over AL, with the transmitted pulse around 0.010 μs, shallow interfaces in the first 0.050 μs and the bedrock interface visible around 0.18 μs. All A-scan times are raw measurements and hence two-way delays.

software, available from `https://sourceforge.net/projects/proexgprcontrol/`, was used to collect 4095 samples at a rate of at least 10 times the nominal center frequency. The measurement settings included a sampling rate of 7694 MHz, selected to maximize the number of samples per period and yet map the deepest bedrock interfaces – defined as the surface between two layers – after a two-way trip delay of 532 ns estimated from preliminary investigations. Each trace collected was georeferenced using a C/A GPS L1 receiver at a constant time interval of 0.5 s. The altitude information was not accurate enough for topographic correction due to a limited view of the satellite constellation when working on the slopes, so the horizontal position information was used to sample a DEM over the track location. Considering a latitude-longitude uncertainty of 5 m and a maximum slope of 37°, the resulting altitude uncertainty is 4 m. The DEM was created from a pointcloud collected with a LiDAR scanner located on the Haavimbfjellet summit. This location is also where the picture shown in Fig. 3 was shot from, with an excellent coverage of the Slåttofjellet slopes.

The GPR B-scans were generated and processed using custom GNU/Octave scripts also available from the authors at `https://sourceforge.net/p/proexgprcontrol/code/ci/master/tree/octave_scripts/`. The process involved the following steps:

1. The raw A-scan records, stored as analog to digital converter arbitrary unit values, were read for post-processing. We define fast time axis the time along each A-scan (in our case, from 0 to 532 ns), while the slow time axis is determined by the pulse repetition interval as the operator is walking up and down the slope. In our case, each new A-scan acquisition is separated by 0.5 s.

2. The mean value of each A-scan was removed so that further processing is not affected by any mean value offset (e.g. artifact during cross-correlation analysis and boundary effects during filtering).

3. A band-pass filter with a band-pass from 100 to 800 MHz was applied to each A-scan, with cutoff frequencies below 60 MHz and above 840 MHz.

4. A linear gain was applied along the fast time axis, starting from the emitted pulse origin.

5. The altitude on the 2010 DEM provided by NPI [34] corresponding to the data collection location was identified for each A-scan. A virtual time delay equivalent to the GPR altitude is introduced before the 0 A-scan time to reflect varying topography, assuming a wave velocity of 170 m/μs over the whole B-scan. The 170 m/μs velocity, corresponding to a relative permittivity of the dielectric medium of 3, matches the top-most layer assumed to be mostly ice, neglecting the thin rock layer overlaying the buried ice.

6. Position interpolation was performed to generate a B-scan map with equidistant traces, despite the varying distance between data collection points.

The 532 ns fast-time window was selected, following preliminary investigation to roughly assess the maximum delay introduced by the deepest features, to map interfaces up to 45 m deep. The deepest features are only visible in B-scans 7 and 8 (Fig. 5) when reaching the main glacier body, and no interface was missed in the slopes.

No migration processing was applied to these data beyond the signal processing steps described above since only smooth interfaces are investigated and a constant velocity was assumed for all sub-surface media. The GPS position derivate was used to assess the operator's velocity and interpolate the periodically collected GPR A-scans at a constant space interval along the elevation profiles as the final processing step. Indeed due to variations in terrain steepness, the operator's speed could not be constant, resulting in faster walking on flat areas compared to climbing or walking down 35-37° slopes: interpolating the A-trace location at constant intervals along the slow-time axis when assembling the B-scans eases further analysis and display in a matrix data representation.

To tow the entire setup, an operator used a mountaineering deadman anchor to install a hauling system. This system was used both for pulling the equipment on the way up and for slowing it on the way down. Data reproducibility was assessed by recording tracks both on the way up and on the way down.

The DEMs were created from georeferenced LiDAR scans obtained annually from 2012 to 2021 using a Riegl VZ-6000 instrument. However, only the first and last datasets collected in the snow-free period of Autumn were used for this analysis. Registration of the scans was achieved using an Iterative Closest Point Algorithm implemented in the Riegl RiSCAN Pro software [35]. The 2010 DEM [34], with a resolution of 5×5 m, served as a reference. The LiDAR data was rasterized using CloudCompare software at a resolution of 1×1 m [36].

5 Results

All the radargrams that were obtained could be displayed in the context of their collection environment (Fig. 4) and interpreted as shown on Figs. 5 and 6. The transects were labeled in a sequence starting from transect 1 downstream and ending at transect 8 upstream. These transects show the evolution of the slope structure from the outer moraine (transect 1) to the area still covered by glacier ice further upstream (transect 8). The purpose of this acquisition procedure was to determine how the ice remaining buried in the slopes under debris – here called buried ice –. develops spatially and assess its connection to the main body of the glacier.

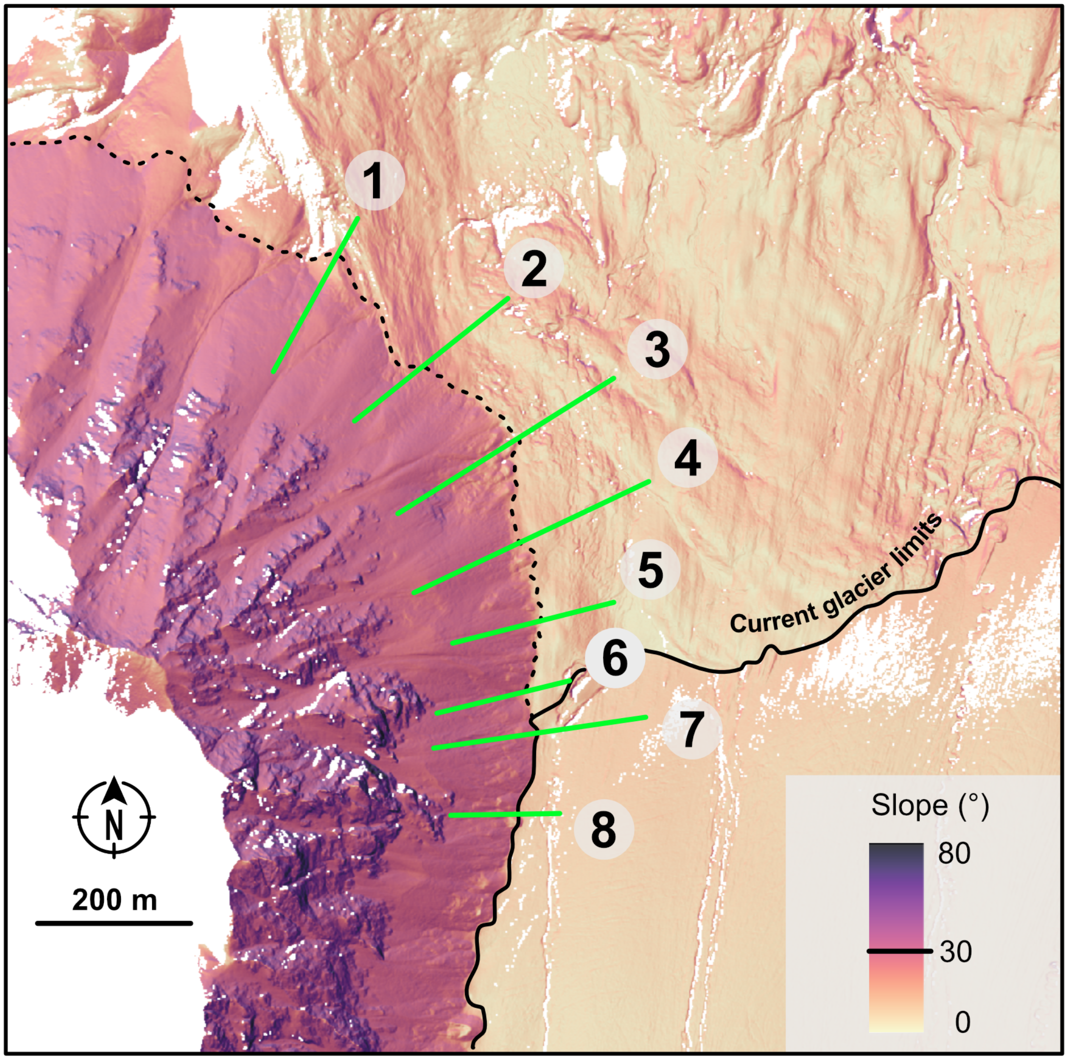

Figure 4: Location of the GPR transects (green lines). The background image is a DEM with color encoding of the slope from flattest (light) to steepest (dark). The reference to a slope angle of 30° in the legend indicates the threshold above which avalanches are triggered.

The analysis of the B-scans confirms the suitability of the selected measurement locations, as they all showed a blurred, shallow interface above a well-defined deep interface. Since GPR maps sub-surface dielectric interfaces, the shallow blurred interfaces are associated with a dense concentration of scatterers (boulders, rocks mixed in ice). The blurred aspect of the shallow reflectors is interpreted as multiple, overlapping hyperbolas, whose individual contribution to the globally reflected signal cannot be separated.

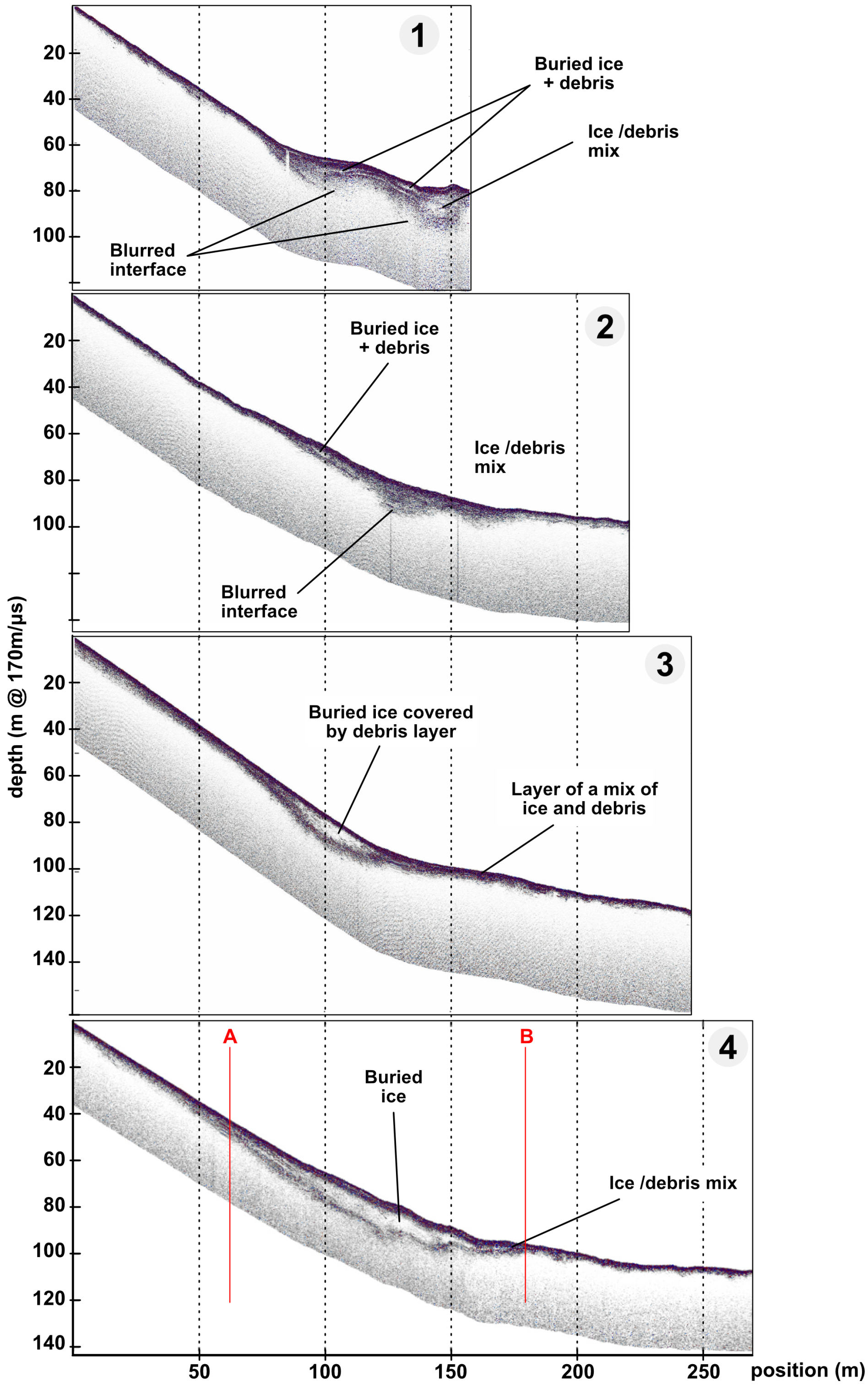

Figure 5: B-scan radargrams collected along transects 1 to 4, furthest from the current glacier position.

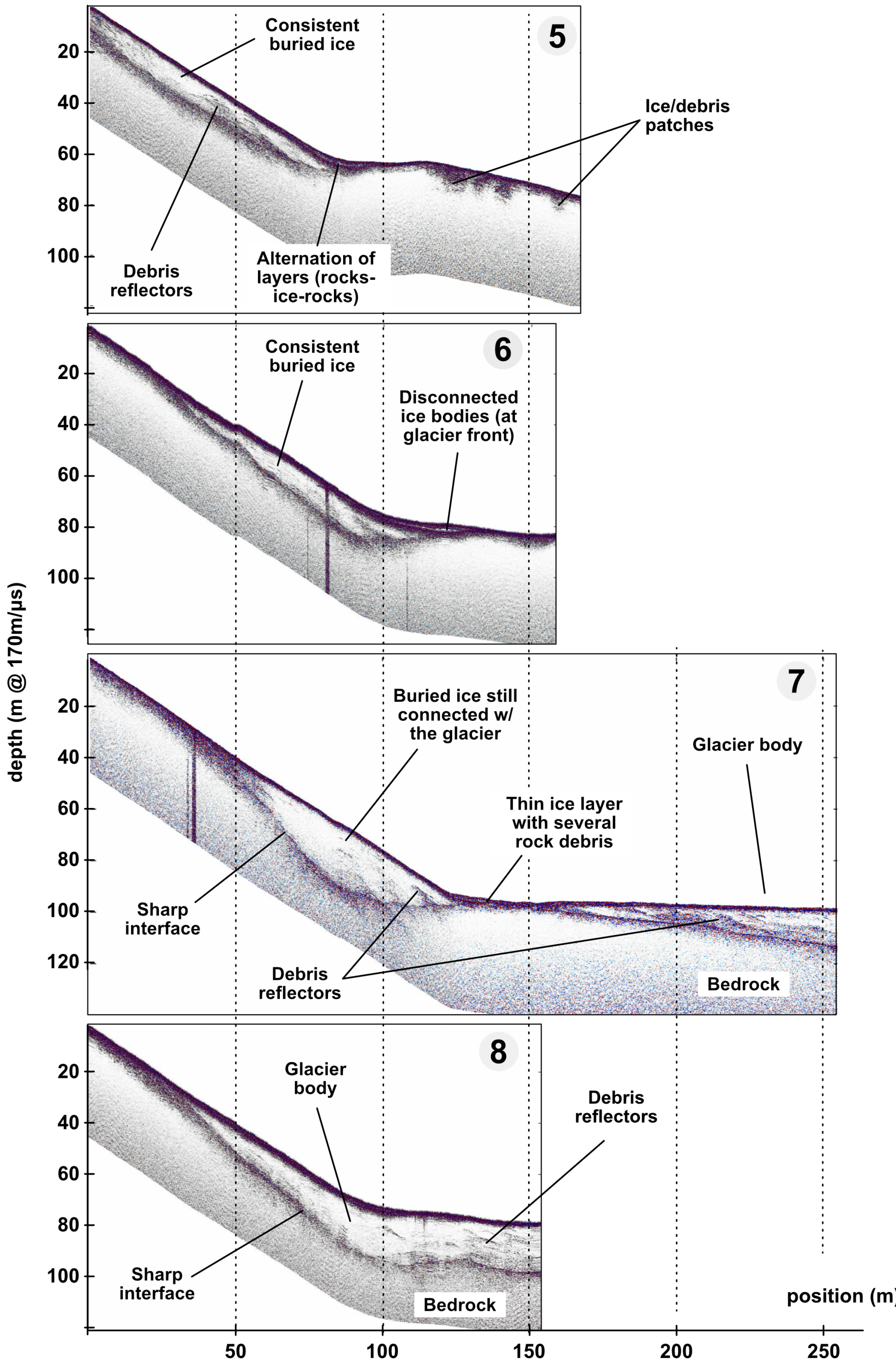

Figure 6: B-scan radargrams collected along transects 5 to 8, closest to the current glacier position.

The B-scan areas lacking reflectors are associated with homogeneous media, whether ice or rock. The sharp, deepest and high amplitude, interface is associated with the ice-bedrock boundary.

One particular B-scan, taken along the flow direction of the glacier from its surface to the moraine, helped interpret the deepest, sharp interface seen on the B-scans, as the boundary between ice and the bedrock. This transect, which is shown in supplementary material S1, also confirmed that the ice thickness vanishes at the visible ice-moraine boundary, which defines the current extent of the glacier. Transect 7 was intentionally chosen to reach the glacier front, where the sharp interface in the slope disappears and a new sharp interface appears over the glacier to the right of the B-scan, representing the ice-bedrock interface. Upstream, transect 8 displays a continuous sharp interface from upstream to the glacier surface, providing evidence that:

1. The deeper sharp interface visible in all B-scans collected in the slopes are ice layers buried under the rock debris that is visible from the surface.

2. This ice buried in the slopes is connected to the main glacier ice body.

These results are consistent with previous findings from [27], and transect 8 was purposely conducted to connect the new findings with the earlier ones.

The shallow blurred interface, which is most visible on transect 1 where the deeper sharp interfaces are not visible, corresponds to the interface between the debris on the surface and the buried ice. This interface is expected to exhibit chaotic and high intensity patterns, also qualified as blurred above, due to the mixture of ice and debris with a gradient in the content of rock and ice, rather than a sharp interface separating the ice and the bedrock. As stated earlier, each scatterer is the source of an hyperbolic reflection, but the high density of scatterers leads to overlapping hyperbolas whose individual contribution is no longer identified and interfere with each other.

Since GPR operates as a pulse generator with a broad frequency range [37, 38], the effective transmitted waveform center frequency is determined by the fixed antenna geometry and the varying relative permittivity of the surroundings, despite the commericial identification of the antennas by a frequency characteristic (so-called 500 MHz shielded antennas). The bowtie antenna width of 30 cm – or half-wavelength – leads to an electromagnetic wavelength of approximately 60 cm over ice with a relative permittivity of 3, resulting in an electromagnetic velocity of 170 m/μs and a center frequency of around 300 MHz under these conditions. When this wave reaches higher permittivity layers such as rock, e.g. with a relative permittivity of 5, its wavelength drops to 45 cm since frequency remains constant in linear media. In our experiments, the A-scans show a received pulse centered on 390 MHz, identified as the maximum of the power spectrum of the recorded signals, corresponding to a wavelength in ice of 170/390 or 44 cm. Hence, subsurface features with dimensions on the order of, or smaller, than this wavelength are detected on the B-scans as blurred interfaces due to scattering [39, 40], including boulders and ice lenses in the decimeter range, while larger reflectors would appear as discrete hyperbolas from strong point-like reflectors. All media being linear, the wavelength in each medium determines the largest structure below which scattering rather than reflection defines the interaction of the electromagnetic wave with the sub-surface debris. The transmitted, propagating wave and received signal will necessarily all have the same frequency determined by the relative permittivity around the transmitter for a given bowtie antenna geometry.

6 Discussion

Starting from the areas closest to the current position of the glacier snout, transect 8 demonstrates the continuous connection of the buried ice in the slopes with the main glacier body, in agreement with past observations [27]. Transect 7 was designed to intersect the buried ice body under the slopes with the current front of the glacier.

From the altitude of the buried ice volumes in transects 8, 7 and 6, we consider the buried ice body to be continuous under the slopes. Fig. 7 provides an interpretation of the measurement results including an extrapolation of the ice extent (solid yellow line) under the debris at the feet of the Slåttofjellet slopes, highlighting how transect 7 is at the limit of the glacier front and helps interpreting the sharp deep interface in all radargrams. The dashed yellow lines indicate areas where extrapolation is uncertain due to missing measurement data.

Based on both radargrams and field observations, we may deduce that AL can be seen as a debris-covered glacier type thank to the supply of debris from the surroundings topography. Indeed, in this glacier type, debris supplied processes mainly are i) rockfalls or avalanches from surrounding hillslopes, directly onto the ablation area and ii) slumping from the lateral moraine [41]. These 2 points are observed over AL. Furthermore, it corresponds with the general trend of glacial retreat that comes with an increasing extent of debris cover on glacier tongues [42]. This particular point is a common feature found over many glaciers on Brøgger peninsula.

From this analysis, we conclude that the highest extent of the buried ice in the slopes is representative of the latest maximum extent of the glacier, with the highest ice being the oldest and the first to have been

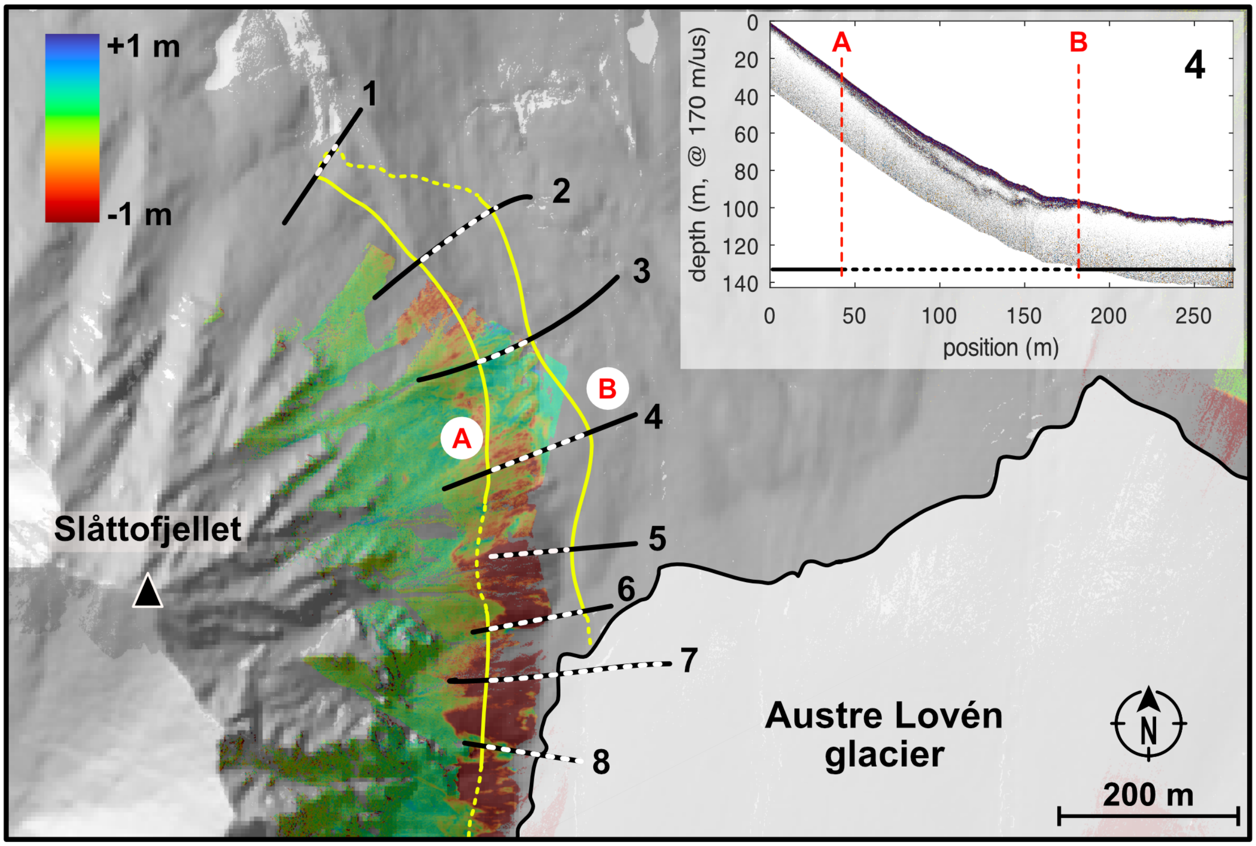

Figure 7: Buried ice extent (yellow solid line) deduced from the highest and lowest intersection of the deeper sharp interface (dashed lines of each transect) with the surface along each GPR transect (see inset, top-right, for the case of transect 4, see Fig. 5), mapped over the current glacier extension (solid gray, bottom-right) and the hillshade DEM on the background overlaid with the Difference of DEMs between 2012 and 2021 (colored, red is a lower altitude in 2021 than in 2012).

buried under falling debris as the glacier was melting and retreating (Fig. 8). As the glacier was retreating, transect 1 was certainly the first to be debris covered and to seem disconnected from the glacier. As the retreat continued, the areas where the next transects are located were subject to similar processes. We observe that the highest ice extent in the slopes lies 40±10 m above the current ice elevation of the exposed glacier surface. Past estimates [28] account for about 0.45 m water-equivalent/year ice loss since 1962 or 0.5 m/year ice thickness loss. The extrapolation of climatic proxies [43] indicates lower loss values during the first half of the 20th century. These results are consistent with a melt of the glacier by 50 m at most during the century since the picture of Fig. 1 was shot. The ice buried in the slopes is a remnant of this past ice extent.

From the difference of DEM maps, we observe that the lowest part of the slopes has evolved over the last decade, losing up to about 1 m between 2012 and 2021, while the upper parts of the slopes are observed

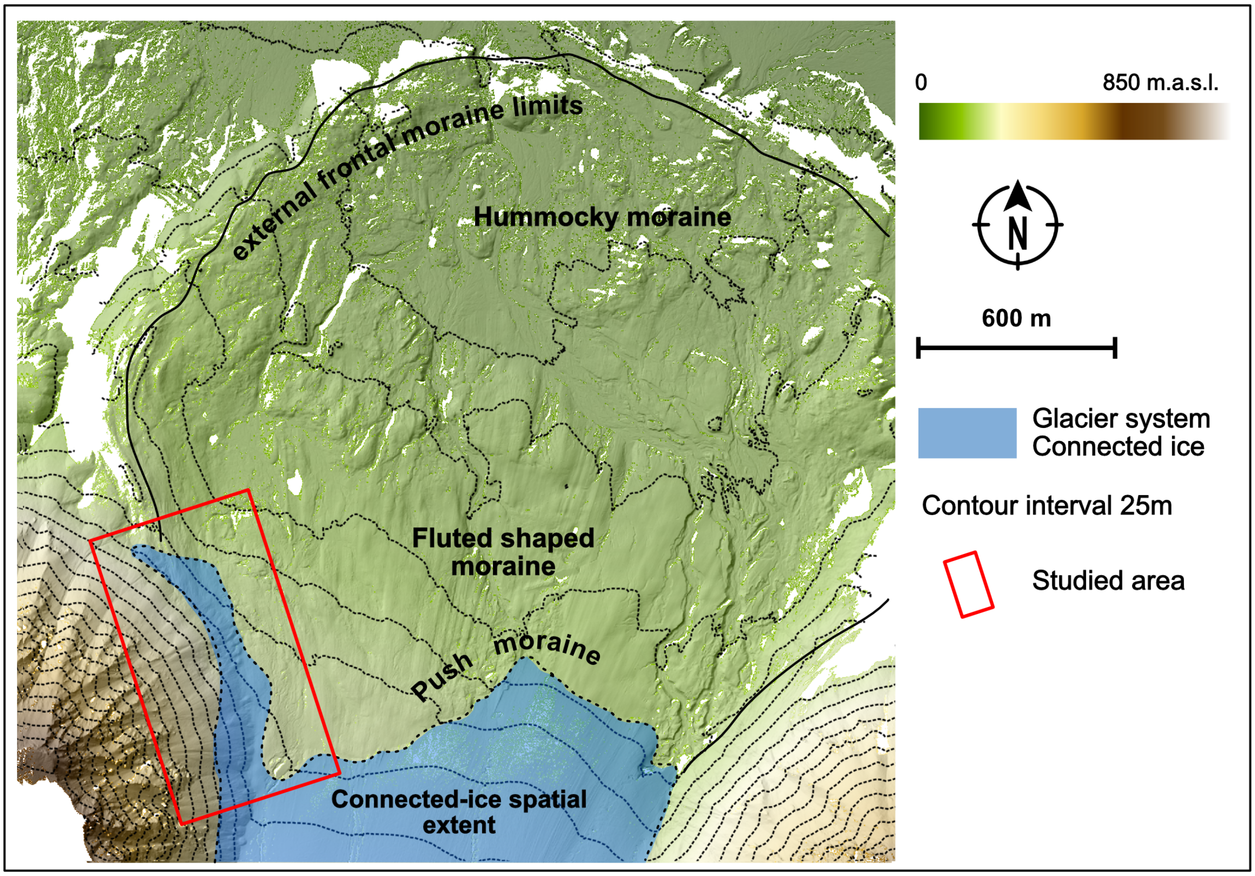

Figure 8: Left bank ice extent (blue) deduced from the highest and lowest intersection of the deeper sharp interface with the surface along each GPR transect overlaid on an elevation color encoding and level lines separated by 25 m. The studied area is highlighted by the red rectangle.

to remain at constant elevation (Fig. 7). We interpret this difference in behavior of the older, upper buried ice, and the lower, newer buried ice, as follows. Amongst the processes associated to a debris-covered glacier formation, supraglacial debris alter underlying ice ablation rates. Depending on the debris layer thickness, a tradeoff between heat transfer by the dark surface increasing melt rates and thermal insulation decreasing melt rates will create a gradient in the buried ice thickness evolution [44] in addition to impacting slope dynamics, geometry, and hypsometry [45].

According to [46], several parameters impact the ice melt rate in the slopes with regard to the debris surface properties including conductivity, moisture content, and roughness. The evolution of debris cover is controlled by i) melt-out of englacial debris and ii) redistribution by ice flow. However, AL is characterized by a low ice-flow rate [47], vanishing at the bottom of the slopes. As a result, the buried ice has reached equilibrium in the upper slopes where melt no longer reduces the ice thickness now protected by a thick debris layer, while the lower parts of the slopes are still subject to melting under the thinner debris layer acting as a heating surface. Similar to the upper slopes of transects 8 to 4, the ice observed under the slopes of transects 3 to 1 no longer melts thanks to the thicker debris layer inducing a slowdown of sub-debris ice ablation [48].

Considering the increase of debris over the glacier due to the increased activity of the slopes (i.e. landslides, debris flow, avalanche events), one goal of this paper was to focus on the glacier effective extent. Fig. 8 connects all ice bodies by extrapolating the boundary to both the main AL glacier and the connected ice in the slopes. This emphasizes how higher the old glacier expanded with respect to its current extent if we consider the buried ice as remnant of an historical thicker, larger glacier. The interpretation of the ice interaction with the slopes is highlighted on Fig. 9 where the convex ice body of the growing glacier shrinks to a concave bank shape when the glacier is shrinking and the remaining retreating ice close to the slopes is covered with rock debris. This type of shape favors the formations of swales between the glacier and the slopes, leading to bediere formation.

Fig. 9 illustrates the processes described above, with the rock debris falling from the slopes covering the buried ice, hence protected from melting as the main body of the glacier melts in the context of worldwide glacier retreat. While this process was only observed on one surrounding mountain slope, Slåttofjellet, similar ice-core features are visible under rockslides on the opposite Haavimbfjellet slopes (supplementary material S2), although the latter site is not accessible for safety reasons to the same experimental assessment on ice-core thickness in the slopes using GPR. Indeed, the right bank shape led to lateral bediere formation which prohibits easy access. We hence tentatively extend our conclusions on ice-cored slopes surrounding the glacier basin up to an altitude representative of past glacier extension to the whole basin.

The 8 transects used in this study do illustrate the successive stages glaciated slopes go through as the AL glacier is retreating over time.

7 Conclusion

Based on our initial observations of fan-shaped landforms that suggest the presence of ice bodies in the slopes surrounding a small Arctic glacier, we used Ground Penetrating RADAR to map the sub-surface features in areas that are still connected to the glacier and areas that have become disconnected as the glacier retreated. We observed a distinct boundary between the underlying rocks and the ice core, indicating the presence of a bedrock, as well as a less defined boundary caused by rock debris covering the ice bodies and preventing

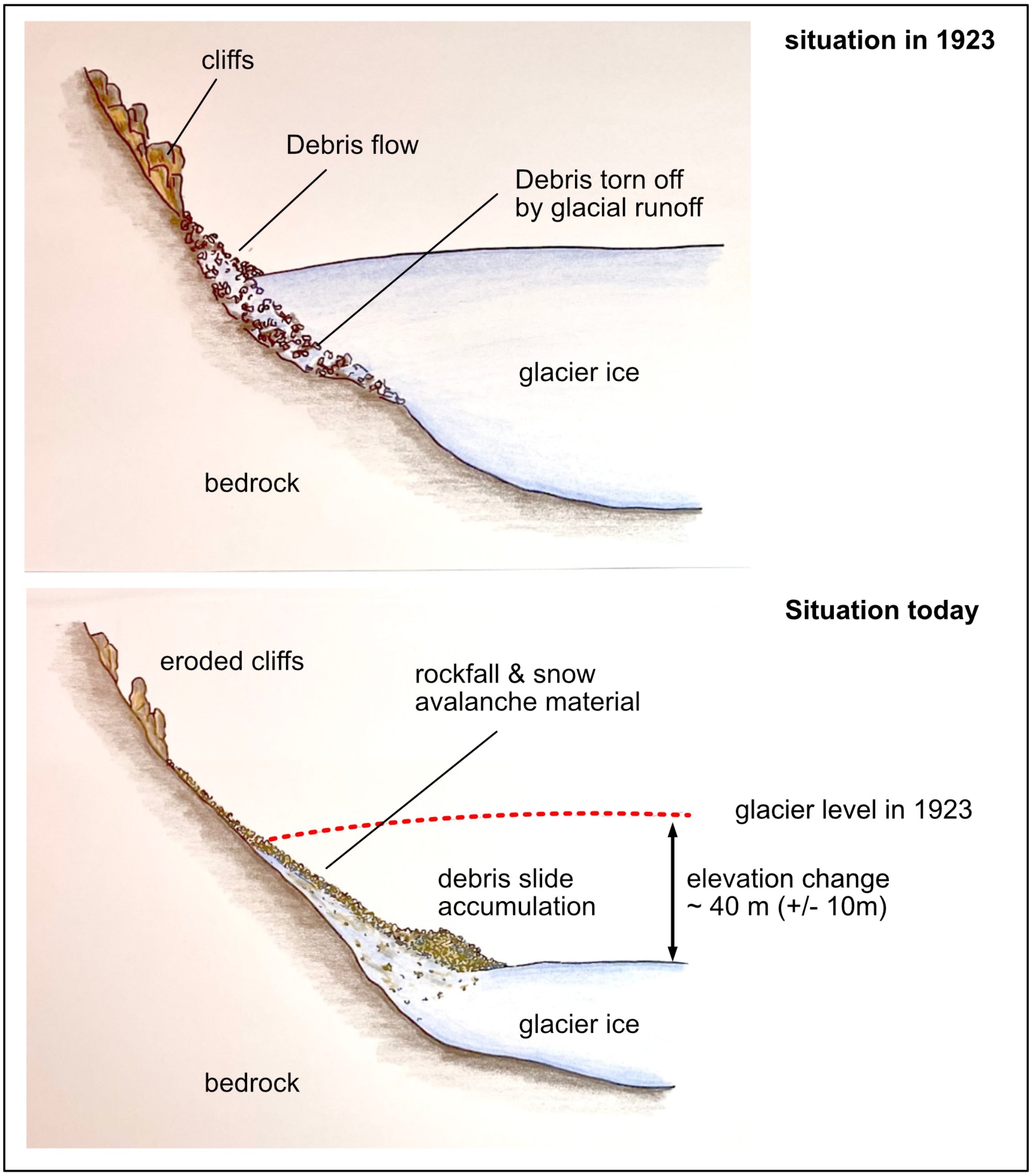

Figure 9: Illustration of the glacier retreat and adjustment of slopes. The talus deposits were altered, revealing the subsurface ice layer and burying AL at the bottom of the slope. As the glacier retreated, the sides collapsed and swallowed a portion of the glacier ice. Ultimately, the main scarp's backward erosion concealed the ice that was exposed. This sketch summarizes our best interpretation of the GPR B-scans and matches the layout of transect 8.

further melting. By analyzing the extent of these ice-cored slopes, we can infer that the glacier extended to a higher altitude, approximately 30 to 50 m above its current location. In addition, the observation of the radargrams presented here provides evidence of the successive stages in the evolution of ice-cored slopes subsequent to glacier retreat.

This work contributes in mapping ice extent beyond the visual exposed bare ice body by observing subsurface buried ice in the slopes. These buried ice volumes are protected from melt by layers of rock debris until a mixture of ice and rock is formed as seen downstream in the oldest parts of the slopes surrounding the main glacier body.

Acknowledgement

This work is supported by the French polar institute IPEV (Institut Paul Émile Victor) and the Franche-Comté County through their research grant.

References

[1] T. N. Tonkin, N. G. Midgley, S. J. Cook, and D. J. Graham. Ice-cored moraine degradation mapped and quantified using an unmanned aerial vehicle: A case study from a polythermal glacier in Svalbard. *Geomorphology*, 258:1–10, 4 2016.

[2] Hanne H. Christiansen, Ole Humlum, and Markus Eckerstorfer. Central Svalbard 2000–2011 meteorological dynamics and periglacial landscape response. *Arctic, Antarctic, and Alpine Research*, 45:6–18, 2 2013.

[3] J. Putkonen and M. O'Neal. Degradation of unconsolidated Quaternary landforms in the western North America. *Geomorphology*, 75(3-–4):408–419, May 2006.

[4] Sven Lukas, Lindsey I. Nicholson, and Ole Humlum. Comment on Lønne and Lyså (2005): "Deglaciation dynamics following the Little Ice Age on Svalbard: Implications for shaping of landscapes at high latitudes", geomorphology 72, 300–319. *Geomorphology*, 84:145–149, 2 2007.

[5] E. Serrano, M. Oliva, M. González-García, J.I. López-Moreno, J. González-Trueba, R. Martín Moreno, M. Gómez-Lende, J. Martín-Díaz, J. Nofre, and P. Palma. Post-little ice age paraglacial processes and landforms in the high Iberian mountains: A review. *Land Degradation and Landforms*, 29(11):4186–4208, November 2018.

[6] Jasper Knight, Stephan Harrison, and Darren B. Jones. Rock glaciers and the geomorphological evolution of deglacierizing mountains. *Geomorphology*, 324:14–24, 1 2019.

[7] N. G. Midgley, T. N. Tonkin, D. J. Graham, and S. J. Cook. Evolution of high-arctic glacial landforms during deglaciation. *Geomorphology*, 311:63–75, 2018.

[8] Ireneusz Sobota. Icings and their role as an important element of the cryosphere in high arctic glacier forefields. *Bulletin of Geography, Physical Geography series*, 10:81–93, 2016.

[9] J.-B. Bosson, P. Deline, X. Bodin, P. Schoeneich, L. Baron, M. Gardent, and C. Lambiel. The influence of ground ice distribution on geomorphic dynamics since the little ice age in proglacial areas of two cirque glacier systems. *Earth Surface Processes and Landforms*, 40(5):666–680, April 2015.

[10] Marie-Françoise André. Geomorphic impact of spring avalanches in Northwest Spitsbergen (79° N). *Permafrost and Periglacial Processes*, 1:97–110, 1990.

[11] Marie-Françoise André. Holocene rockwall retreat in Svalbard: a triple-rate evolution. *Earth Surface Processes and Landforms: The Journal of the British Geomorphological Group*, 22(5):423–440, 1997.

[12] Denis Mercier, Julien Coquin, Thierry Feuillet, Armelle Decaulne, Etienne Cossart, Helgi Pall Jónsson, and Porstein Sæmundsson. Are Icelandic rock-slope failures paraglacial? Age evaluation of seventeen rock-slope failures in the Skagafjördur area, based on geomorphological stacking, radiocarbon dating and tephrochronology. *Geomorphology*, 296:45–58, 11 2017.

[13] M. Church and J. M. Ryder. Paraglacial sedimentation: A consideration of fluvial processes conditioned by glaciation. *GSA Bulletin*, 83:3059–3072, 1972.

[14] Colin K. Ballantyne. Paraglacial geomorphology. *Quaternary Science Reviews*, 21:1935–2017, 10 2002.

[15] Colin K. Ballantyne. A general model of paraglacial landscape response. *The Holocene*, 12:371–376, 4 2002.

[16] Olav Slaymaker. Proglacial, periglacial or paraglacial? *Geological Society, London, Special Publications*, 320:71–84, 1 2009.

[17] Olav Slaymaker. Criteria to distinguish between periglacial, proglacial and paraglacial environments. *QUAGEO*, 30:85–94, 1 2011.

[18] Marek W. Ewertowski and Aleksandra M. Tomczyk. Quantification of the ice-cored moraines' short-term dynamics in the high-Arctic glaciers Ebbabreen and Ragnarbreen, Petuniabukta, Svalbard. *Geomorphology*, 234:211–227, 2015.

[19] Colin K. Ballantyne and Douglas I. Benn. Glaciological constraints on protalus rampart development. *Permafrost and Periglacial Processes*, 5:145–153, 8 1994.

[20] A. M. Curry, V. Cleasby, and P. Zukowskyj. Paraglacial response of steep, sediment-mantled slopes to post-'little ice age' glacier recession in the central Swiss Alps. *Journal of Quaternary Science*, 21:211–225, 3 2006.

[21] Ida Lønne and Astrid Lyså. Deglaciation dynamics following the Little Ice Age on Svalbard: Implications for shaping of landscapes at high latitudes. *Geomorphology*, 72:300–319, 2005.

[22] Katja Laute and Achim A. Beylich. Influences of the Little Ice Age glacier advance on hillslope morphometry and development in paraglacial valley systems around the jostedalsbreen ice cap in Western Norway. *Geomorphology*, 167-168:51–69, 9 2012.

[23] Denis Mercier, Samuel Étienne, Dominique Sellier, and Marie-Françoise André. Paraglacial gullying of sediment-mantled slopes: a case study of Colletthøgda, Kongsfjorden area, West Spitsbergen (Svalbard). *Earth Surface Processes and Landforms*, 34:1772–1789, 10 2009.

[24] Annett Bartsch, Martin Gude, and SD Gurney. Quantifying sediment transport processes in periglacial mountain environments at a catchment scale using geomorphic process units. *Geografiska Annaler: Series A, Physical Geography*, 91(1):1–9, 2009.

[25] Matthias Benjamin Siewert, Michael Krautblatter, Hanne Hvidtfeldt Christiansen, and Markus Eckerstorfer. Arctic rockwall retreat rates estimated using laboratory-calibrated ERT measurements of talus cones in Longyeardalen, Svalbard. *Earth Surface Processes and Landforms*, 37(14):1542–1555, 2012.

[26] Tjalling De Haas, Maarten G Kleinhans, Patrice E Carbonneau, Lena Rubensdotter, and Ernst Hauber. Surface morphology of fans in the high-Arctic periglacial environment of Svalbard: Controls and processes. *Earth-Science Reviews*, 146:163–182, 2015.

[27] É. Bernard, J.M. Friedt, A. Saintenoy, F. Tolle, M. Griselin, and C. Marlin. Where does a glacier end? GPR measurements to identify the limits between valley slopes and actual glacier body. Appli-

cation to the Austre Lovénbreen, Spitsbergen. *International Journal of Applied Earth Observation and Geoinformation*, 27:100–108, 4 2014.

[28] Christelle Marlin, Florian Tolle, Madeleine Griselin, Eric Bernard, Albane Saintenoy, Mélanie Quenet, and Jean-Michel Friedt. Change in geometry of a high Arctic glacier from 1948 to 2013 (Austre Lovénbreen, Svalbard). *Geografiska Annaler: Series A, Physical Geography*, pages 1–24, 2 2017. doi: 10.1080/04353676.2017.1285203.

[29] W. Mittelholzer. Kingsbai mit Kingsgletscher und Lovenfirnen von Osten aus 1700 m, 1923. `https://commons.wikimedia.org/wiki/Category:ETH-BIB_Mittelholzer-Spitsbergen_flight_1923`.

[30] A Hamberg. En resa til norra Ishafet sommaren 1892. *Ymer*, 14:25–61, 1894. `https://paleoarchive.com/literature/Hamberg1894-ResaNorraIshafvet.pdf`.

[31] N. G. Midgley and T. N. Tonkin. Reconstruction of former glacier surface topography from archive oblique aerial images. *Geomorphology*, 282:18–26, 2017.

[32] Georgina L. Bennett and David J A Evans. Glacier retreat and landform production on an overdeepened glacier foreland: The debris-charged glacial landsystem at Kvíárjökull, Iceland. *Earth Surface Processes and Landforms*, 37:1584–1602, 2012.

[33] Tadeusz Głowacki and Damian Kasza. Assessment of morphology changes of the end moraine of the Werenskiold glacier (SW Spitsbergen) using active and passive remote sensing techniques. *Remote Sensing*, 13, 2021.

[34] Norwegian Polar Institute. Terrengmodell Svalbard (S0 Terrengmodell) data set, 2010. `https://publicdatasets.data.npolar.no/kartdata/S0_Terrengmodell/Delmodell/NP_S0_DTM5_2010_13828_33.zip`.

[35] RIEGL Laser Measurement Systems. Riscan pro – version 2.1.1, 2015.

[36] Cloudcompare (version 2.12), 2023. http://www.cloudcompare.org/.

[37] D. Rabus, F. Minary, G. Martin, and J.-M. Friedt. A high-stability dual-chip GPR for cooperative target probing. In *IEEE GPR Conference*, Rapperswil, Switzerland, 2018.

[38] J.-M. Friedt, G. Martin, G. Goavec-Merou, D. Rabus, S. Alzuaga, L. Arapan, M. Sagnard, and É. Carry. Acoustic transducers as passive cooperative targets for wireless sensing of the sub-surface world: Challenges of probing with ground penetrating RADAR. *MDPI Sensors*, 18(1):246, 2018.

[39] I. Santin, G. Roncoroni, E. Forte, P. Gutgesell, and M. Pipan. GPR modelling and inversion to quantify the debris content within ice. *Near Surface Geophysics*, pages 1–15, 2023.

[40] S. Franke, T. Gerber, C. Warren, D. Jansen, O. Eisen, and D. Dahl-Jensen. Investigating the radar response of englacial debris entrained basal ice units in East Antarctica using electromagnetic forward modelling. *IEEE Transactions on Geoscience and Remote Sensing*, 61:4301516, 2023.

[41] A Lambrecht, C Mayer, Wilfried Hagg, V Popovnin, A Rezepkin, N Lomidze, and D Svanadze. A comparison of glacier melt on debris-covered glaciers in the northern and southern Caucasus. *The Cryosphere*, 5(3):525–538, 2011.

[42] Dirk Scherler, Hendrik Wulf, and Noel Gorelick. Global assessment of supraglacial debris-cover extents. *Geophysical Research Letters*, 45(21):11–798, 2018.

[43] B Lefauconnier and JO Hagen. Glaciers and climate in Svalbard: statistical analysis and reconstruction of the Brøggerbreen mass balance for the last 77 years. *Annals of Glaciology*, 14:148–152, 1990.

[44] Natalya V Reznichenko, Tim RH Davies, and David J Alexander. Effects of rock avalanches on glacier behaviour and moraine formation. *Geomorphology*, 132(3-4):327–338, 2011.

[45] Evan S Miles, Ian C Willis, Neil S Arnold, Jakob Steiner, and Francesca Pellicciotti. Spatial, seasonal and interannual variability of supraglacial ponds in the Langtang Valley of Nepal, 1999–2013. *Journal of Glaciology*, 63(237):88–105, 2017.

[46] Leif S Anderson and Robert S Anderson. Debris thickness patterns on debris-covered glaciers. *Geomorphology*, 311:1–12, 2018.

[47] Songtao Ai, Xi Ding, Jiachun An, Guobiao Lin, Zemin Wang, and Ming Yan. Discovery of the fastest ice flow along the central flow line of austre lovénbreen, a poly-thermal valley glacier in Svalbard. *Remote Sensing*, 11, 2019.

[48] Lindsey I Nicholson, Michael McCarthy, Hamish D Pritchard, and Ian Willis. Supraglacial debris thickness variability: impact on ablation and relation to terrain properties. *The Cryosphere*, 12(12):3719–3734, 2018.